Significant role of physical transport in the marine carbon monoxide (CO) cycle — Observations in the East Sea (Sea of Japan), the Western North Pacific, and the Bering Sea in summer

Young Shin Kwon[1], Tae Siek Rhee[2]*, Hyun-Cheol Kim[2], Hyoun-Woo Kang[1]

5 [1]Korea Institute of Ocean Sciences and Technology, Busan, 49111, Korea
[2]Korea Polar Research Institute, Incheon, 21990, Korea

Correspondence to: Tae Siek Rhee (rhee@kopri.re.kr)

Abstract. The carbon monoxide (CO) in the marine boundary layer and in the surface waters and water column were measured along the Northwestern Pacific limb from Korean Peninsula to Alaska, U.S.A. in summer 2012. The observation allows us to

10 estimate the CO budgets in the surface mixed layer of the three distinct regimes, the East Sea (ES), the Northwest Pacific (NP), and the Bering Sea (BS). Microbial consumption rates were $33(\pm22)$ μmol m^{-2} day^{-1}, $23(\pm11)$ μmol m^{-2} day^{-1}, and $77(\pm32)$ μmol m^{-2} day^{-1}, and CO production rates were $70(\pm49)$ μmol m^{-2} day^{-1}, $20(\pm11)$ μmol m^{-2} day^{-1}, and $19(\pm7)$ μmol m^{-2} day^{-1} in ES, NP and BS, respectively, both of which are the dominant components of the CO budget in the ocean. The other two known components, air-sea gas exchange and downward mixing remain negligible (less than 2 μmol m^{-2} day^{-1}) in all regimes. While

15 the CO budget in the surface mixed layer of NP is in balance, the CO production surpassed the consumption in ES and vice versa in BS. The significant imbalances in the CO budget in ES and BS requires external physical transport such as lateral advection, subduction, or ventilation. Indeed, the first order increase of the CO column burden to the extent that the imbalance in the CO budget increases points to the significant play of the physical transport in the CO cycles. Our observation, for the first time, points to the potential importance of physical transport in the marine CO cycle.

1 Introduction

Carbon monoxide (CO) plays a key role in the budget for the hydroxyl (OH) radical in the atmosphere (Weinstock and Niki, 1972; Levy, 1971), which indirectly contributes to global climate change as a considerable range of greenhouse gases, including methane (CH_4), are oxidized by the OH radical in the atmosphere (Daniel and Solomon, 1998). The ocean has long been recognized as a source of atmospheric CO, albeit with large uncertainties in its source strength (1 − 190 Tg CO yr-1)

25 (Conte et al., 2019; Erickson Iii, 1989; Bates et al., 2012; Conrad et al., 1982; Rhee, 2000; Stubbins et al., 2006; Zafiriou et al., 2003), which requires further investigation and understanding of the CO cycle in the ocean.

In the euphotic zone of the ocean, CO is produced by abiotic photochemical reaction of chromophoric dissolved organic matter (CDOM). Annual global CO photoproduction in the ocean is estimated to be in the range of 10 − 400 Tg CO (Mopper and Kieber, 2000; Zafiriou et al., 2003; Kitidis et al., 2006; Fichot and Benner, 2011; Erickson Iii, 1989; Conrad et al., 1982), with

30 a large span of uncertainty that could be attributed to the heterogeneous distribution of CDOM in the world ocean. As the second largest inorganic carbon product after CO_2 in photochemical conversion of the dissolved organic carbon, CO itself draws considerable attention as a key proxy to evaluate the photoproduction of CO_2 and bio-labile organic carbon (Mopper and Kieber, 2000; Miller et al., 2002; Armbrust, 2009). Thus, CO is a noteworthy component with regard to both the oceanic carbon cycle and global climate change.

35 CO in the water column is removed by microbial consumption, air-sea gas exchange, and vertical dilution, with microbial consumption being the dominant sink under normal turbulent conditions at the ocean's surface. Microbial consumption rates of CO range from 0.003 to 1.11 h⁻¹ depending on locality and season (Conrad and Seiler, 1980; Conrad et al., 1982; Johnson and Bates, 1996; Jones, 1991; Jones and Amador, 2012; Ohta, 1997; Xie et al., 2005; Zafiriou et al., 2003). As mentioned above, dissolved CO in the surface ocean is generally supersaturated with respect to the atmospheric CO concentration (Seiler,

40 1974) leading to sea-to-air emission (Conrad and Seiler, 1980). Physical mixing within the surface mixed layer ends up diluting the CO concentration in water column when it is deeper than the light penetration depth, beyond which photoproduction is no longer possible (Gnanadesikan, 1996; Kettle, 2005).

Estimating the ocean source strength remains challenging due to the large uncertainties in the budget of marine CO. Although recent modelling studies have attempted to estimate the CO flux from the ocean surface at the global scale (Conte et al., 2019),

45 these estimates are limited by the large uncertainties in the budget and may be biased in shallow continental shelf regions. Despite the efforts of introducing a new production pathway, namely dark production, in order to rationalize the discrepancy between modelled and observed oceanic CO source strength (Xie et al., 2005; Li et al., 2015; Kettle, 2005), the occurrence of the dark production at global scale is still under debate (Zafiriou et al., 2008). Identifying the missing components in the CO budget is essential for predicting the dynamic feedback between oceanic CO level and global climate change with greater

50 confidence.

To better understand the CO dynamics in distinct marine environments, we conducted a study of the CO distribution in water column and overlying air, the microbial consumption rate, and the CDOM absorbance. In this study we reported a CO budget

estimated from these observations and onboard experiments, and compared them with the column burden of CO to examine the control factors on the distribution of CO in the water column. To our knowledge, this is the first systematic study of CO

55 budget in the region of the western limb of the North Pacific.
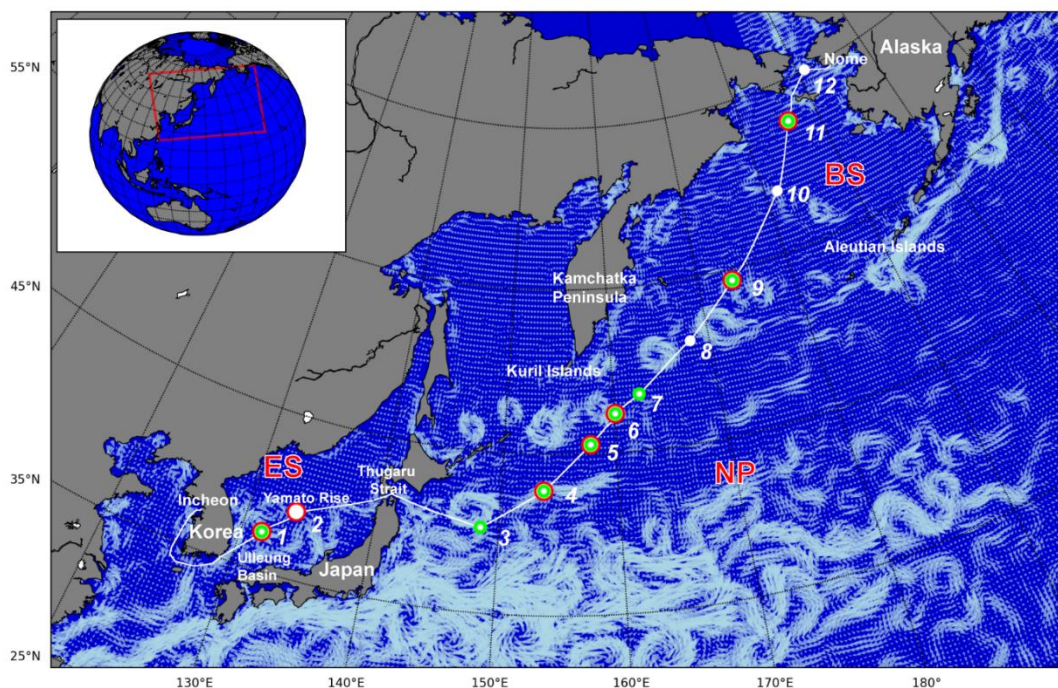
Figure 1: Cruise track (white line) and hydrographic stations (white dot) occupied during the SHIPPO expedition. Dark incubation experiments were conducted at the locations marked by red circles, and CDOM absorbance was measured at the locations marked by green circles. The white arrows on the map designate surface mean currents in July 2012, as taken from OSCAR (Ocean Surface Current Analysis Real-time) database. The red square in the inset indicates the study area.

2 Materials and Methods

2.1 Expedition

The SHIpborne Pole-to-Pole Observations (SHIPPO) expedition was carried out onboard R/V Araon from Incheon, Korea, to Nome in Alaska, U.S.A., over two weeks in 2012 (Figure 1). The cruise track covered the coast surrounding the Korean Peninsula and three ocean provinces: The East Sea (Sea of Japan) (ES), the western limb of the North Pacific (NP), and the Bering Sea (BS). For this study, we focused on the oceanic properties relevant to the marine CO cycle in ES, NP, and BS, and thus excluded the coastal regions around Korean Peninsular and near Nome, Alaska, in defining the ocean province (see Figure 2). Along the cruise track, we occupied two hydrographic stations in ES—one on the northern fringe of the Ulleung Basin between the islands of Ulleung-do and Dokdo Islands and the other on Yamato Rise—six stations in NP spreading from the east of the Tsugaru strait to the western Aleutian Islands, and three stations in BS—one at the Bering slope, another in the inner shelf, and the other nearby the port in Nome. We excluded station 12 from the BS province, as it is too close to the coast to represent the oceanographic properties of the Bering Sea. The expedition covers characteristic marginal seas, ES and BS, and open ocean of NP.

2.2 Underway CO measurements

A commercially available instrument RGA-3 (Reduced Gas Analyzer-3; Trace Analytical Inc.) was used to analyze CO with an automated analytical system (Rhee, 2000). The ambient air at 29 m above sea level was withdrawn through ~100 m long polyethylene inner-coated aluminium tubing (DEKABON) by a pump (KNF, N026ATE) for atmospheric CO analysis. No contamination from the media has been attested. Seawater inlet was mounted on the sea chest locating ~7 m below the sea surface. Seawater was pumped into a typical shower-type Weiss equilibrator in which dissolved CO in the seawater was dynamically equilibrated with the CO in the headspace, which was then delivered to the analyzer. The equilibrator was made of opaque polytetrafluoroethylene (Teflon™) and seated in the laboratory. Seawater was continually showered through the headspace at ~30 L min^{-1}, resulting in the equilibration time of 40 minutes for CO (Rhee, 2000). The ambient air and the headspace air in the equilibrator were sampled every 45 minutes. To keep the analyzing system from being wet, a water trap (Sicapent™) was mounted in front of the automated CO analyzing system. No alteration of CO concentration due to mounting the water trap was detected.

2.3 Dissolved CO concentrations in discrete samples

Dissolved CO concentrations in the discrete samples of each hydrographic station were determined by static equilibrium technique (Rhee, 2000). Seawaters were subsampled in glass jars from the Niskin samplers fired at given depth. Known amount (50 mL) of ultra-pure N_2 gas (99.9999%) was collected using a gas-tight syringe after passing through Schuetze reagent which oxidize CO to CO_2 effectively. This CO-free N_2 was injected into the glass jars to make headspace. After being shaken vigorously, the glass jars were placed in a thermostat at 20°C for about 1 hour to reach the equilibrium between the headspace

and the seawater of dissolved CO. Then, the air in the headspace was analyzed by the same analytical system as used for underway measurement with manual injection. Dissolved CO concentration, C_w, was determined based on the conservation of the dissolved CO concentration in the seawater sample collected in the jar by the following equation (Rhee et al., 2007).

$$C_w = \frac{x_{CO} \times (P - P_w)}{\rho_w RT} \times \left(\beta \times \frac{T}{273.15} + \frac{V_h}{V_w} \right) \tag{1}$$

90 , where x_{CO} represents the dry mole fraction of dissolved CO, P the ambient pressure, P_w saturated water vapour pressure, ρ_w the density of seawater at a given temperature, R gas constant, T absolute temperature at the sampling time of dissolved gas, β Bunsen solubility coefficient, V_h volume of the headspace, and V_w volume of the seawater.

2.4 Determination of microbial oxidation rate

Dark incubation experiments were conducted onboard at selected stations to determine the microbial oxidation rate coefficient
95 of CO (k_{CO}) in unfiltered seawater samples collected in the surface mixed layer. Four aliquots of seawater were subsampled in glass jars from a Niskin bottle at each station (red circles in Figure 1). The glass jars were wrapped with colored cellulose film to block light during sampling and were stored in an aquarium where the surface seawater was continually supplied to maintain the same temperature as that in the surface mixed layer. Dissolved CO concentrations in the glass jars were measured at regular intervals, and an exponential-decay fitting function was applied to determine k_{CO} at the given stations.

100 ### 2.5 CDOM analysis

Approximately 200 mL of seawater was subsampled in an amber glass container from Niskin bottle at selected stations (lime circles in Figure 1). The seawater sample was filtered through 0.45 μm filter paper (Advantec). Absorption spectra of the filtrate were obtained using a spectrophotometer (Agilent Cary-100) by scanning wavelength from 350 to 800 nm. Milli-Q water was used as a reference blank. Baseline offset was corrected by subtracting the average apparent absorbance from 600
105 to 700 nm from each spectrum (Green and Blough, 1994).

CDOM absorbance obtained from the instruments onboard was converted to absorption coefficient (a_c) by Beer-Lambert law. Previous studies demonstrated the exponential decay of a_c with increase of wavelength in the region of ultraviolet and visible light, which can be represented by a_c at a reference wavelength, λ_0, and spectral slope, S (Bricaud et al., 1981). These two characteristic parameters can be determined by fitting to the following exponential form,

$$a_c(\lambda) = a_c(\lambda_0) * e^{-S(\lambda - \lambda_0)} \tag{2}$$

110 We chose the reference wavelength of 412 nm which is often used in the remote sensing community as a representative of CDOM absorption in the ocean. $a_c(412)$ by CDOM was proven to be a typical linear relation with the CDOM absorption at other wavelength (Mannino et al., 2014). In addition, this wavelength is often chosen to correct the absorption by CDOM to

derive Chl-*a* in remote sensing (e.g., Carder et al., 1999) or to compare the spectral slopes in the CDOM absorption obtained in various regions (e.g., Twardowski et al., 2004) .

2.6 Ancillary measurements

Wind speed was measured by an anemometer (R.M. Young Co. Model 05106-8M) installed on the foremast at 29 m above sea level. It was corrected for ship speed and direction to obtain true wind speed (Smith et al., 1999) and then converted to the neutral wind speed at 10 m above sea level of standard height using the bulk air-sea flux algorithm COARE 3.6 (Edson et al., 2013; Fairall et al., 2003). Solar irradiation was measured with an Eppley Precision Spectral Pyranometer (model PSP) integrating radiation over 285−2800 nm. The surface Chl-*a* concentration was measured by a fluorometer (Turner Designs 10-AU) supplying the surface seawater continuously. The values were adjusted to the Chl-*a* concentration determined by a Trilogy Laboratory Fluorometer (Turner Designs) according to the standard procedure described by Parsons et al. (1984). Sea surface temperature (SST) and salinity (SSS) was logged using both a thermosalinograph (SBE-45, Seabird) mounted in the laboratory and a pair of thermometers (SBE-38) mounted on the seawater inlet of the sea chest.

2.7 Calculation of the CO budget terms

Assuming that lateral advection of CO is negligible, dissolved CO concentration ([CO]) in the mixed layer, *h*, was determined by the sum of the rates of photochemical production (*J*), air-sea gas exchange (*F*), vertical diffusion (*V*) across bottom of the mixed layer, and microbial oxidation (*M*):

$$h\frac{d[\text{CO}]}{dt} = J + M + F + V \tag{3}$$

We assume dark production (Zhang et al., 2008) or other unknown processes including production from particulate carbon and emission by phytoplankton (Duarte and Regaudie-De-Gioux, 2009; Kowalczuk et al., 2010; Zafiriou et al., 2008) to be negligible in the CO budget. We calculated daily budget terms of CO in the surface mixed layer at the stations based on our observed data. Here we defined one day as sum of half a day before and after the time of CTD cast (gray strip in Figure 2). The CO budget terms were integrated over the mixed layer at the given station. Mixed layer depth (MLD) was determined at the shallowest depth below reference depth of 10 m at which the density difference exceeds the density at the reference depth due to temperature difference of 0.2°C (De Boyer Montégut, 2004).

2.7.1 Photochemical production (*J*)

The photochemical production rate (*J*) was determined by product of irradiance, the amount of CDOM, and apparent quantum yield (ϕ_{CO}) of CDOM, an indicator of the CO production efficiency. Since CDOM is not a chemical compound but rather a moiety of material defined by mechanical criterion, ϕ_{CO} varies depending on a variety of conditions. *J* can be mathematically described as follows:

$$J = \int_{z=0}^{z=\infty} \int_{\lambda_{min}}^{\lambda_{max}} I_0(\lambda, 0^-) e^{-k_d(\lambda)z} \times a_c(\lambda, z) \times \emptyset_{CO}(\lambda, z) \, d\lambda \, dz \qquad (4)$$

, where $I_0(\lambda, 0^-)$ indicates monochromatic solar irradiance just beneath the air-sea interface, $k_d(\lambda)$ diffuse attenuation coefficient, $\emptyset_{CO}(\lambda, z)$ apparent quantum yield of CO. Parentheses in Equation 4 indicates function of variables, *i.e.*, λ wavelength and z water depth.

We measured irradiance in the short-wavelength range onboard, but not individual monochromatic wavelengths. Thus, a model
145   calculation by Tropospheric Ultraviolet and Visible radiation (TUV) model (www2.acom.ucar.edu) was employed to resolve the irradiance of monochromatic wavelength between 290 nm and 700 nm. The total irradiance from TUV was normalized to the observed irradiance to estimate the irradiance on the sea surface. To obtain $I_0(\lambda, 0^-)$, sea surface albedo was calculated following Sikorski and Zika (2012). To apply for the equations, direct and diffuse spectral incident irradiance was obtained by the Bird model (Bird and Hulstrom, 1981):

$$f_{abs} = f_{dir}[(1.03 - A_{dir})(1 - f_{ice}) + f_{ice}] + f_{dif}\left[(1.03 - A_{dif})(1 - f_{ice}) + f_{ice}\right] \qquad (5)$$

$$A = 1 - f_{abs} \qquad (6)$$

150   , where *f* and *A* represent fraction and Albedo, and subscripts, *abs*, *dir*, and *dif*, indicate absorption of sunlight and direct and diffuse spectral incident irradiance, respectively. Then, we obtained the normalized irradiance as follows:

$$I(\lambda, 0^-) = I(\lambda, 0^+) \times A \qquad (7)$$

$$I_0(\lambda, 0^-) = I(\lambda, 0^-) \frac{I_{obs}}{I(\lambda, 0^+)} \qquad (8)$$

, where $I(\lambda, 0^+)$ indicates the irradiance calculated by TUV model, $I(\lambda, 0^-)$ and $I_0(\lambda, 0^-)$ represent irradiance beneath the air-sea interface with and without normalization using the observed irradiance, I_{obs}.

Diffuse attenuation coefficient, $k_d(\lambda)$, was determined by following the algorithm in Sikorski and Zika (2012). It takes into
155   accounts not only absorption and scattering coefficients of seawater and particles including phytoplankton, but also reflectance of direct and diffuse spectral radiation in the water column.

Not measuring apparent quantum yield ($\emptyset_{CO}$), we applied two parameterization determined by Zafiriou et al. (2003) and Stubbins et al. (2011) in order to determine photochemical production rate (*J*). The former is derived from the measurement in the surface seawater of the open ocean in the Pacific and the latter from the composite of estuarine and the Atlantic
160   observation. In general Stubbins et al. (2011) parameterization results in approximately twice as much as that using Zafiriou et al. (2003) as the former basically relies on the terrestrial CDOM.

2.7.2 Microbial oxidation (M)

Microbial oxidation rate was determined by a first-order reaction kinetics of a product of dissolved CO concentration and k_{CO} determined at the given station as follows:

$$M = k_{\mathrm{CO}} \times C_w \tag{9}$$

165 In case of incubation experiment not being conducted, mean value of k_{CO} determined in the given geographic province was adopted.

2.7.3 Air-sea flux (F)

Based on the underway observations of CO in the surface seawater (C_w) and in the overlying air (C_a), we calculated air-sea CO flux (F) as follows:

$$F = k_{\mathrm{w}} \times (C_w - LC_a) \tag{10}$$

170 , where k_{w} and L represent gas transfer velocity and the Ostwald coefficient of solubility (Wiesenburg and Guinasso, 2002), respectively. k_{w} is a function of wind speed and the Schmidt number (Sc). We employed three different parameterizations of k_w; (Wanninkhof, 2012) (W92), (Nightingale et al., 2000) (N00), and Wanninkhof (2014) (W14) parameterizations (Table 1). Ho et al. (2011) compiled the entire dual tracer experiments to precisely parameterize gas transfer velocity and concluded their parameterization is virtually same as Nightingale et al. (2000) within the uncertainties. Wanninkhof (2012) parameterization

175 has been used widely and it may hint the potential maximum contribution of air-sea flux to the CO budget.

As all the parameterizations are based on Sc of 600 (Nightingale et al., 2000) or 660 (Wanninkhof, 2012) which is for CO_2 at 20°C in fresh water or in seawater, we normalized Sc to that for CO at the *in situ* temperature and salinity:

$$k_w = k(Sc_{\mathrm{CO}}/Sc)^{-1/2} \tag{11}$$

, where k is the parameterizations of CO_2 gas transfer velocity, Sc_{CO} represents the Schmidt number for CO. We derived a parameterization of Sc_{CO} as a function of both temperature and salinity since its parameterization in literature (e.g., Zafiriou et

180 al. (2008)) considers temperature only (Text S1 in supporting information).

2.7.4 Vertical diffusion (V)

The vertical diffusion rate (V) was determined as the product of vertical eddy diffusivity (K_z) and vertical gradient of CO at the bottom of the mixed layer. K_z was derived from a one-dimensional General Ocean Turbulence Model (GOTM) that was forced by ECMWF reanalysis data (ERA5) and relaxed toward observed temperature and salinity vertical profiles at each

185 station (Kwon et al., 2021).

3 Results

3.1 Oceanographic settings of the provinces

3.1.1 The East Sea (Sea of Japan) (ES)

The Tsushima Warm Current (TWC) dominates the upper water column of the southern part of ES carrying eddies along the
190   main current and flows out through Tsugaru Strait (Kim and Yoon, 1996; Isobe, 2002). In spite of originating from the Kuroshio Current carrying salt and heat from the western part of the Equator branching in the southwestern part of Japanese archipelago, its physical properties are slightly modified in the East China Sea by mixing with fresh water flowing from Yangtze River (Morimoto et al., 2009; Isobe, 2002).

Highest SST of 22.4°C and SSS of 34 were registered in ES among the values observed along the cruise track, showing the
195   dominant influence of TWC on the surface waters (Figure 2f). The southern part of ES often develops warm eddies due to meandering of TWC horizontally (Isoda and Saitoh, 1993), which could be revealed by high salinity and warm water in the Ulleung Basin near Station 1 and Yamato Rise around Station 2. On the other hand, the North Korea Cold Current flows southwards from near Vladivostok along the east coast of the Korean peninsula, which was detected on July 15 with 1°C lower temperature (22.5°C) and 2−3 lower salinity (< 32) than TWC. Approaching the Tsugaru Strait in ES a slight decreasing
200   tendency in SST from ~22°C to ~20°C and increasing tendency in SSS from 33.5 to 33.8 were recorded. This is due likely to higher latitude of the Tsugaru Strait than the inlet of TWC, the Korea Strait, and to the branching and meandering of TWC in ES. Upon entering the mouth of the Tsugaru Strait, SST fell by 4°C from ~21.5 in spite of nearly constant or slight decrease in SSS by ~0.5 pointing to the sudden change in the water mass crossing the strait due likely to the influence of the Oyashio currents from the North Pacific (Yasuda, 2003).
205   Because of the oligotrophic characteristics of the TWC (Kwak et al., 2013), Chl-*a* concentration in the surface along the ship track were lower than 0.5 mg m^{-3} except for the coastal area near the Korean peninsula (Figure 1). MLDs at the stations 1 and 2 were nearly 12 m (Table 1).

3.1.2 The North Pacific (NP)

The NP province is governed by the Western Subarctic Gyre (WSAG), which is operated by both its western boundary currents
210   and the Subarctic Current: the former is composed of the East Kamchatka and the Oyashio Currents, flowing off the Kamchatka Peninsula, Kuril Islands, and Hokkaido southward (Yasuda, 1997), and the latter returns to the northeast merging into the Kuroshio Extension (Kawai, 1972). The Subarctic Current is bounded by and mixes with the Kuroshio Extension forming the Subarctic Front south to WSAG. This front extends from the Kuroshio-Oyashio Confluence region off the Hokkaido where the Kuroshio Extension and the Oyashio current are mixing.
215   Leaving the Tsugaru Strait, SST remained almost constant at 16–17°C, while SSS fluctuated between 32.5 and 33.5 indicating mixing of the weak Oyashio Current and the strong Kuroshio Extension in the offshore of the Hokkaido, where the Kuroshio-Oyashio confluence region is located and the Subarctic Current forms along the Subarctic Front (Yasuda, 1997). This Subarctic

Front covers Stations 3 and 4 until 154.6°E in front of Kuril islands, where the SST and SSS suddenly decrease by 6°C from 16.5°C and by 1 from 33.6, respectively, indicating entry into the WSAG (Yasuda, 1997) (Figure 1 and 2). In the WSAG, SST

220 and SSS remained almost constant at 9°C and 32.8, respectively. Approaching Station 8, SST and SSS slightly increased by ~1°C and 0.2, respectively, alluding crossing of a warm core ring. As WSAG crosses the Aleutian islands (Kuroda et al., 2021), we extended the NP province to Station 9.

WSAG is known as high nutrient low chlorophyll (HNLC) region where primary production is thought to be limited by the availability of dissolved iron (Fujiki et al., 2014). This is reflected in the higher variability (0.2 mg m^{-3}) and mean value of

225 Chl-*a* concentration (0.9 mg m^{-3}) in NP compared to the marginal seas, ES and BS (Figure 1 and Table 1). The MLD at NP stations ranges from 11 – 14 m, except for Stations 5 and 9 where MLDs were 20 m and 22 m, respectively. Excluding these two stations, the mean MLD is similar to that in ES, but it would deepen to 14.5 m if including both stations.

3.1.3 The Bering Sea (BS)

The Bering Sea is a marginal sea separated from the North Pacific by Commander and Aleutian Islands. In spite of geographical

230 separation, WSAG extends the Bering Basin mainly through Kamchatka and Nier Straits, circulates cyclonically along the Bowers Ridge and Shirshov Ridge, and returns to the North Pacific through Kamchatka Strait flowing by the Kamchatka Current (Stabeno et al., 1999). Thus, we extended the North Pacific province over Station 9 (Figure 2).

Upon crossing the longitude 176.4°E on July 25, salinity increased slightly, and dissolved CO concentration suddenly soared, suspecting influence of other water masses. Indeed, the Alaskan Stream flows westwards from the Alaska Gyre, entering the

235 Bering Basin through the Nier Strait and various Aleutian Passes, mostly Amchitka Pass. It then veered cyclonically along the Bering slope toward the Kamchatka Peninsula, forming the Kamchatka Current (Stabeno and Reed, 1994). Upon leaving Station 10, salinity fell from 32.64 to 29.9 in 8 hours, indicating the entrance of different water masses. The inner shelf of BS is dominated by the Alaska Coastal Current, which deliverers fresh and low-nutrient water to BS mainly through Unimak pass, eventually reaching the Beaufort Sea in the Arctic though the Bering Strait (Yamamoto-Kawai et al., 2006; Ladd and Stabeno,

240 2009). Large variation of SSS observed in the inner shelf of BS suggest a heterogeneous spatial distribution and relatively short residence time of the Alaska current before entering the Bering Strait. At Station 12, located near the Bering Strait, SST and SSS were stark different from those observed on the inner shelf. Salinity reached the value observed in the outer shelf, but the temperature was so low at ~1°C suspecting the water mass from the Gulf of Anadyr.

Chl-*a* concentration in the surface waters of BS was lower than that in NP, but similar to that in ES, with a mean value of 0.7

245 mg m^{-3}. However, it significantly increased to over 8 mg m^{-3} near the Alaska coast at Station 12, likely due to the inflow of nutrients from the Gulf of Anadyr. The MLD at the station in the Bering Basin was 19 m, while it shoals to ~12 m at the stations in the continental shelf.

Table 1. Summary of the observed parameters in the different provinces. Data are presented as the average and standard deviation (1σ), with the number of measurements or samples indicated in parentheses.

Properties (units)		East Sea/Sea of Japan	North Pacific	Bering Sea
Air temperature (°C)		20.5 ± 1.3 (85)	12.0 ± 2.8 (140)	7.7 ± 0.5 (91)
Air pressure (hPa)		1008.5 ± 3.9 (85)	1006.4 ± 4.4 (140)	1004.5 ± 4.2 (91)
Relative humidity (%)		84 ± 8 (85)	92 ± 3 (140)	92 ± 4 (91)
U_{10N}[a] (m s^{-2})		6 ± 4 (4791)	9 ± 2 (10151)	8 ± 2 (4663)
Irradiance (MJ m^{-2} d^{-1})		27.0 ± 0.4 (283)	11.8 ± 3.4 (1024)	8.9 ± 4.6 (428)
SST[b] (°C)		21.3 ± 1.9 (4755)	11.8 ± 3.0 (10152)	8.3 ± 0.3 (4662)
SSS[b] (psu)		32.8 ± 1.2 (4755)	32.9 ± 0.3 (10152)	31.9 ± 1.0 (4662)
Chl-a (mg m^{-3})		0.7 ± 0.4 (4752)	0.9 ± 0.3 (10152)	0.7 ± 0.4 (4663)
MLD[b] (m)		11 ± 0.15 (2)	13.9 ± 4.7 (6)	16.5 ± 0.5 (2)
$a_c(412)$[c] (m^{-1})		0.21 (1)	0.16 ± 0.16 (6)	0.17 (1)
k_{CO}[c] (d^{-1})		0.27 ± 0.08	0.13 ± 0.82	0.36 ± 0.7
$[CO]_{sea}$ (nM)		0.5 ± 0.4 (80)	0.6 ± 0.4 (140)	1.6 ± 1.3 (91)
CO_{air} (nmol mol^{-1})		141 ± 38 (85)	112 ± 29 (99)	102 ± 10 (74)
SA[b]		3.1 ± 2.7 (80)	5.0 ± 4.4 (99)	14.3 ± 13.8 (74)
Air-sea CO flux (μmol m^{-2} d^{-1})	W92[d]	0.8 ± 0.9 (80)	2.2 ± 3.0 (99)	6.1 ± 6.7 (74)
	N00[e]	0.7 ± 0.8 (80)	1.7 ± 2.3 (99)	4.8 ± 5.3 (74)
	W14[f]	0.6 ± 0.8 (80)	1.7 ± 2.4 (99)	5.0 ± 5.4 (74)

[a] Neutral wind speed at 10 m high.
[b] SST, SSS, MLD, and SA stand for sea surface temperature, sea surface salinity, mixed layer depth, and saturation anomaly, respectively.
[c] $a_c(412)$ and k_{CO} designate absorption coefficient of CDOM at the wavelength of 412 nm and microbial oxidation constant, respectively.
[d,e,f] Gas transfer velocity parameterizations by Wanninkhof (2012), Nightingale et al. (2000) , and Wanninkhof (2014), respectively.
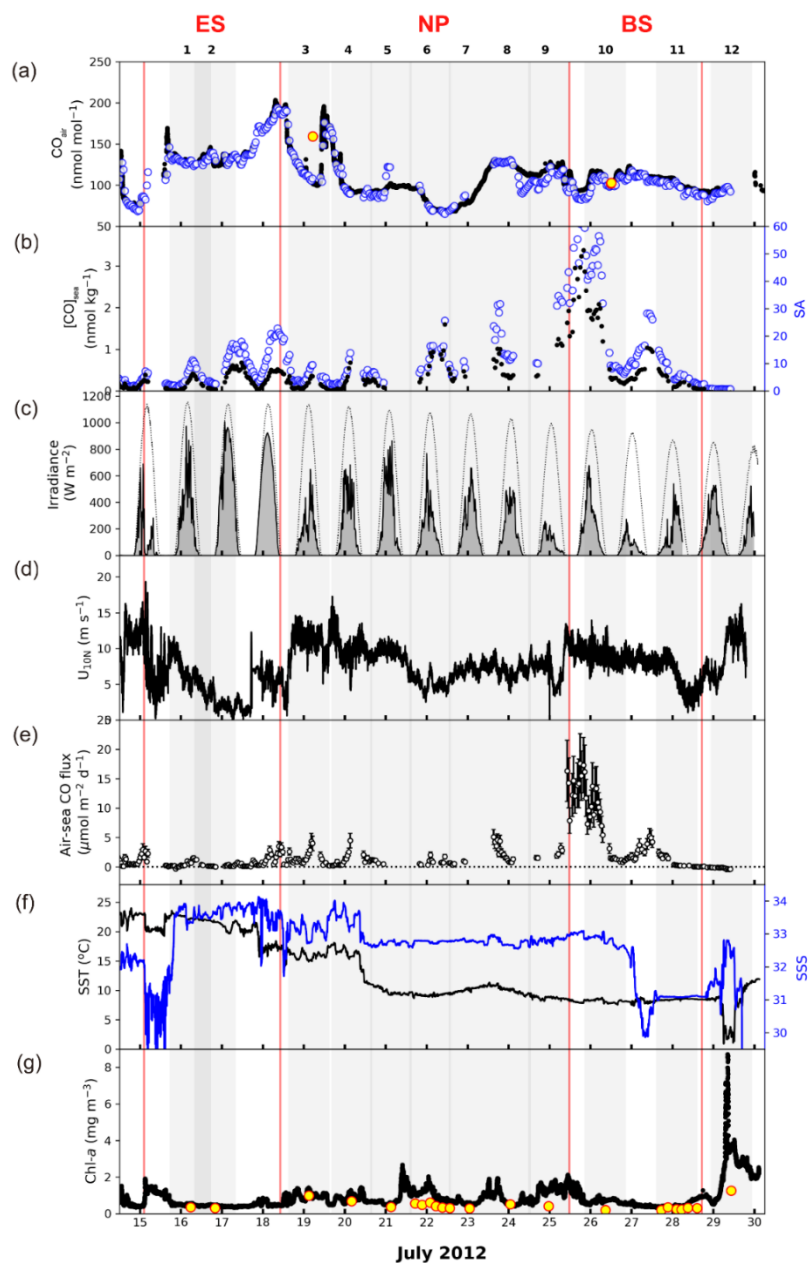
Figure 2: Surface properties observed along the cruise track. (a) mole fractions of CO in the air, (b) dissolved CO concentrations and saturation anomaly in the sea surface mixed layer, (c) observed surface irradiance (thick solid line) and modelled clear-sky irradiance (thin dotted line), (d) neutral wind speed at 10 m high, (e) daily sea-to-air CO flux, (f) SST and SSS, and (g) Chl-*a* concentrations in the surface waters. The time is given in Coordinated Universal Time (UTC). In (a), black circles represent analyses by LGR systems, the blue circles represent RGA-3, and the two red circles filled with yellow represent measurements by NOAA/ESRL at the stations, SHM (Shemya Island, Alaska) and CBA (Cold Bay, Alaska). In (g), black dots represent the continuous measurement by Turner 10-AU fluorometer and red circles filled with yellow indicates the discrete measurements of Chl-*a*. Each gray-shaded area represents one day at each station, and geographical provinces of ES, NP, and BS are separated by vertical red lines.

3.2 Atmospheric situations

270 Air temperature and pressure, and daily insolation generally decreased with increasing latitude (Table 1). Following SST, air temperature was as high as 25°C in the Ulleung Basin of ES and gradually decreased down to 16°C until R/V *Araon* passed the Tsugaru Strait. Upon leaving the strait the air temperature dropped by 7°C and then continued to decrease slowly to 10°C in front of Nome. Air pressure was high in ES (1008 hPa) and low in NP (1006 hPa) and BS (1005 hPa). This pressure gradient along the ship track is visible in the insolation, with cloudy or overcast conditions in NP and BS, and sunny in ES, where the

275 irradiance was greater than twice that in NP and BS (Figure 2c). Wind speed was opposite to the trend of air pressure and insolation, with mean U_{10N} in ES was 6.2 m s^{-1}, approximately 2/3 of that in NP and BS.

3.3 CO in the surface mixed layer and overlying air

During the expedition, atmospheric CO concentration was measured using two different analytical systems. An automated analysis system measured surface CO at the marine boundary layer and surface mixed layer, while an Off-Axis Integrated

280 Cavity Output Spectroscope (Off-Axis ICOS: N_2O/CO analyzer; Los Gatos Research, USA) was used to observe highly resolved variability of CO in the surface marine boundary layer (Park and Rhee, 2015). Difference in atmospheric CO mole fractions between the two analytical techniques was only 5.8 (±6.1) nmol mol^{-1} for this campaign, indicating that our measurements were reliable. We further confirmed our measurements were comparable to the values obtained at the stations run by NOAA/ESRL global network located nearby our cruise track or the same latitudinal zone within a 3- to 5-day time

285 window to our onboard observations (Figure 2a). Atmospheric CO mole fractions (CO_{air}) varied by about 30% with respect to mean value of 118 nmol mol^{-1}, revealing a large variability associated with anthropogenic emissions in the Northern hemisphere (Park and Rhee, 2015). This is further supported by the decreasing trend of provincial mean values as the distance from the anthropogenic source area increases.

Diurnal variation of the dissolved CO concentration ([CO]) in surface waters show a marked fluctuation following solar

290 irradiance, indicating that photochemical production is the main driver (Conrad et al., 1982; Ohta, 1997; Zafiriou et al., 2008). However, this typical diurnal oscillation disappears in the area around the Aleutian archipelago, due probably to overcasting along the cruise track (Figure 2c), and in the Bering Sea with decreasing solar irradiance. Except for July 25 and 26, daily minimum values range from 0.04 nmol kg^{-1} to 0.63 nmol kg^{-1} and maximum values from 0.47 nmol kg^{-1} to 2.09 nmol kg^{-1}, respectively. Along the cruise track, minimum and maximum dissolved [CO] were 0.04 nmol kg^{-1} and 4.6 nmol kg^{-1},

295 respectively, varying over 100% with respect to an average of 0.8 (±0.9) nmol kg^{-1}. The maximum value appeared near the central Bering Sea on July 25. Our mean value is slightly lower than the values observed in other areas due probably to lower productivity evidenced by low Chl-*a* concentration along the cruise track and to the overcast conditions (Figure 2c and g).

3.4 Spectral CDOM absorbance

The optical properties of CDOM can be characterized by its absorption coefficient at a reference wavelength, λ_0 (= 412 nm),
300   denoted by $a_C(\lambda_o)$, and its slope (S) defined in Eq. (2) (Bricaud et al., 1981). $a_c(\lambda_0)$ reflects the CDOM content in the seawater, while S indicates either the source of CDOM or its degradation process. The spectral profile of $a_c(\lambda)$ in surface seawater decreases exponentially with increasing wavelength (Figure 3a). Fitting the raw data into Eq. (2) reveals that the $a_c(412)$ ranged from 0.031 m^{-1} (Station 9) to 0.26 m^{-1} (Station 4). Figure 3b shows that logarithmic values of $a_c(412)$ are inversely correlated with S over the 350–600 nm wavelength range. This inverse relationship is consistent with the observations in the
305   Atlantic Ocean (Kitidis et al., 2006), implying similarities in the biogeochemical properties of CDOM between the Atlantic and Pacific open oceans. Nonetheless, the values of $a_c(\lambda_0)$ and S obtained in this study are relatively high and low, respectively, compared to those in the Atlantic, possibly due to the influence of CDOM sources in the marginal seas adjacent to the Pacific Ocean and relatively short photo-bleaching processes occurring in the open ocean (Brzezinski et al., 2003; Vodacek et al., 1997).

310   The values of $a_c(\lambda)$ at the measured wavelengths showed clear separation into two groups: marginal sea group in ES (Station 1) and BS (Station 11), and open sea group in NP (Stations 5−9). Even though Stations 3 and 4 belong to the NP province, the spectra of $a_c(\lambda)$ at these stations are quite different from those observed at Stations 5 to 9, but are similar to those in ES and BS. This suggests that the composition of CDOM at Stations 3 and 4 should be influenced by the continental sources (e.g., Vodacek et al. (1997)) by means of the Kuroshio Current flowing northward along the Japanese east coast and of the Oyashio
315   Current which meanders in the Okhotsk Sea. As mentioned earlier, the surface waters at Stations 3 and 4 are located in the Kuroshio-Oyashio Confluence Zone as their mean SST (=15.5 ± 0.5°C) and SSS (=33.0 ± 0.4) were higher than those for
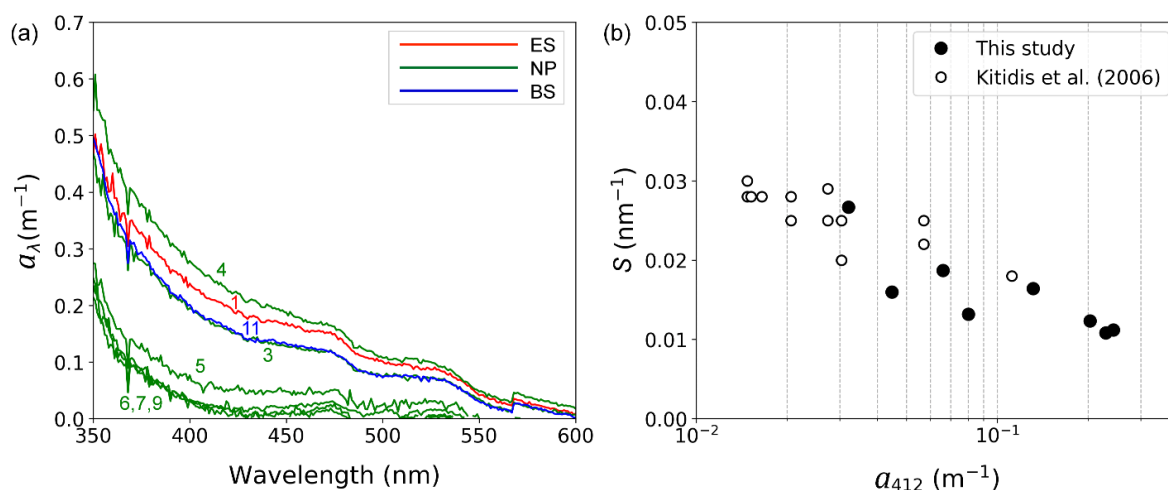
Figure 3: (a) Spectra of CDOM absorption coefficient ($a_c(\lambda)$) in the surface seawater at the given stations and (b) semi-log scatter plot between the spectral slope (S) and the absorption coefficient at the reference wavelength of 412 nm ($a_c(412)$). Numbers in (a) indicate hydrographic stations.

Stations 5–9 by 6.1°C and 0.25, respectively (Figure 2). The $a_c(\lambda)$ spectra are consistent with this physical setting of Stations 3 and 4 (Yamashita et al., 2010; Takao et al., 2014).

320 **3.5 Microbial oxidation rate coefficient**

Figure 4a−c shows the results from the dark incubation experiments carried out onboard. Despite our careful experiments, we do not observe a reduction in dissolved [CO] over time due to microbial oxidation, as would be expected. This could be attributed to various factors, such as an inadequate blank correction, the existence of a threshold [CO] for consumption (Xie et al., 2005), or the possibility of dark production of CO (Li et al., 2015). Nonetheless, we applied a first-order decay function
325 to extract the main trend of CO oxidation, despite the considerable errors caused by the scattered data.

k_{CO} in the surface mixed layer varied from 0.001 hr^{-1} to 0.46 hr^{-1} with an average of 0.22 ± 0.15 hr^{-1} (Figure 4d). Minimum and maximum k_{CO} were observed at Station 9 in NP and at Station 11 in BS, respectively. The mean k_{CO} values in ES, NP, and BS are 0.27 ± 0.07 hr^{-1}, 0.17 ± 0.35 hr^{-1}, and 0.36 ± 0.64 hr^{-1}, respectively. The decrease of the mean k_{CO} values from the marginal seas to the open oceans is consistent with the finding of previous studies, compiled by by Xie et al. (2005), suggesting
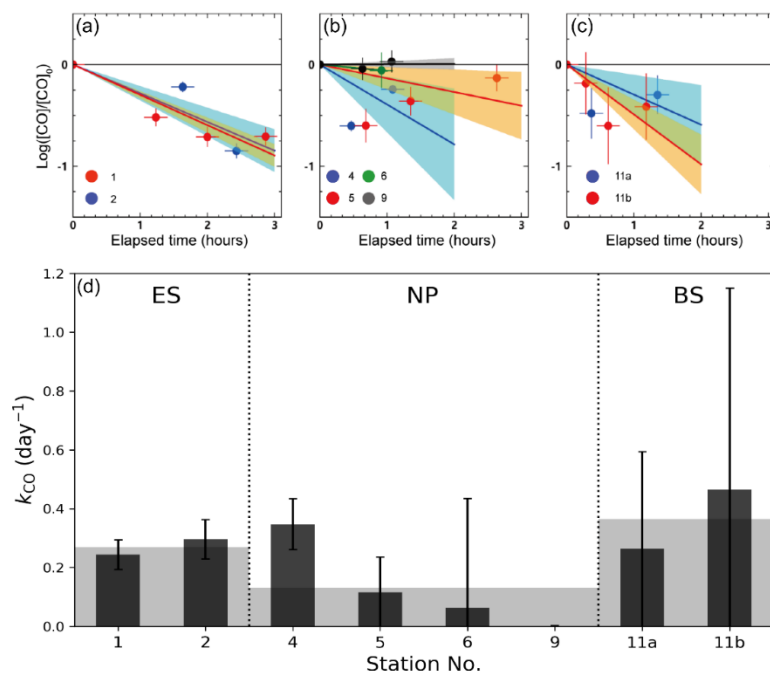
Figure 4: Temporal variation of dark incubation experiment conducted at the stations in (a) ES, (b) NP, and (c) BS, and (d) microbial oxidation rate coefficients (k_{CO}) obtained from the dark incubation experiments. Solid lines and shades in (a) to (C) denote the linear fits and their uncertainties, respectively, and gray shades in (d) indicate the mean values of k_{CO} in the given provinces.

that high Chl-*a* or active primary productivity can serve as an indicator of the activity of CO-oxidizing microbes. Furthermore, Xie et al. (2005) speculated that the high k_{CO} in the Beaufort Sea in their study might reflect the fact that the Arctic Ocean receives large inputs of terrestrial organic carbon favoring the growth of microbial communities. In fact, it was found the considerable fluvial input of organic carbon over the Bering Sea near the Arctic Ocean (Walvoord and Striegl, 2007; Mathis et al., 2005). It could partially explain the higher k_{CO} in the Bering Sea than in the East Sea, despite both being the marginal seas.

3.6 CO budget in the mixed layer

3.6.1 Photochemical production (*J*)

The photochemical production rate would have declined with increasing latitude if it simply depended on the daily integrated insolation (Table 1 and Figure 5). However, provincial mean *J* value in ES was approximately 3.5 times larger than that in NP and BS, while there was little difference between NP and BS due to the high CDOM content in BS (Table 2). The high *J* value in ES is due to a synergetic effect of both high insolation and high CDOM content in the surface seawater. At Stations 3 and 4, the reduced insolation was slightly offset by the high CDOM content (Figure 3a), resulting in a similar *J* value to that at the other stations in NP.

The photochemical production rates of 69 μmol m^{-2} d^{-1} in ES is comparable to those reported in oligotrophic regions, e.g., 68 and 52 μmol m^{-2} d^{-1} in Spring and August, respectively, at BATS (Zafiriou et al., 2008), and 56 and 83 μmol m^{-2} d^{-1} at Southern Pacific Gyre (SPG) and the Pacific equatorial upwelling (PEU) zone, respectively (Johnson and Bates, 1996). On the other hand, the *J* values in NP and BS (~20 μmol m^{-2} d^{-1}) are lower due to declining insolation with latitude and lower CDOM content in NP, as mentioned above (Table 1).

Table 2. Daily mean CO budget (μmol m^{-2} d^{-1}) in the mixed layer of the given provinces

Province	Photochemical production (*J*)	Microbial oxidation (*M*)	Air-sea flux (*F*)	Vertical diffusion (*V*)
East Sea/Sea of Japan	69 ± 49	33 ± 22	0.3 ± 0.1	0.4 ± 0.1
North Pacific	20 ± 11	22 ± 11	2.0 ± 1.7	0.5 ± 0.4
Bering Sea	19 ± 7	77 ± 32	3.7 ± 3.9	1.2 ± 1.4

3.6.2 Microbial oxidation (*M*)

The microbial oxidation rates were highest in the marginal seas of ES and BS, which is mostly attributed to the high k_{CO}, as the mean dissolved [CO] in the provinces were similar (Table 1 and 2). Station 10 had the highest microbial oxidation rate of 100 μmol m^{-2} d^{-1}, while Station 9 showed the lowest value of 0.4 μmol m^{-2} d^{-1}. This result is due to the high k_{CO} and exceptionally high surface [CO] near Station 10 (Figure 2b). By leaving aside Station 9, the *M* values range an order of magnitude with the second lowest value of 16.8 μmol m^{-2} d^{-1} at Station 1, and it does not show any dependence on latitude. Compared to microbial oxidation rates obtained at BATS, SPG, and PEU that ranged from 22 to 45 μmol m^{-2} d^{-1} (Zafiriou et al., 2008; Johnson and Bates, 1996), the high mean value in BS can be attributed to the distinct microbial community structure or biomass of CO-oxidizing species.

3.6.3 Air-sea flux (*F*)

The air-sea CO flux depends on both the [CO] difference between the surface seawater and the overlying air and by gas transfer velocity, mainly driven by wind speed (see Eq. (10)). The former is sometimes transformed to saturation anomaly ($SA = \frac{c_w}{c_a} - 1$; Figure 2b) which directly indicates whether the ocean is a source or sink for atmospheric CO. Throughout the campaign, most of the dissolved CO remained supersaturated, spanning over two orders of magnitude in SA, e.g. –0.6 to 51, resulting in outgassing of CO from the ocean to the atmosphere. Mean SA in provinces increase with latitude due to increase of dissolved [CO] and in part to decrease of atmospheric CO concentration (Table 1).

The daily mean air-sea CO fluxes ranged from –0.1 to 20 μmol m^{-2} d^{-1}, resulting in an average of 2.04 ± 3.76 μmol m^{-2} d^{-1} over the cruise track (Table 1). The mean *F* values of the provinces are, however, quite different, with the lowest value in ES (0.3±0.1 μmol m^{-2} d^{-1}) and the highest in BS (3.7 μmol m^{-2} d^{-1}). In NP, the air-sea flux (2.0±1.9 μmol m^{-2} d^{-1}) is comparable to those observed in the open ocean: 2.2±1.5 and 2.7±1.9 μmol m^{-2} d^{-1} in the North and South Atlantic, respectively (Park and Rhee, 2016); 2.93±2.11 μmol m^{-2} d^{-1} in the oligotrophic Atlantic Ocean (Zafiriou et al., 2008); 2.7 μmol m^{-2} d^{-1} in the oligotrophic equatorial Pacific Ocean (Johnson and Bates, 1996), 1.94 μmol m^{-2} d^{-1} in NP between 30 – 45°N in Summer (Bates et al., 1995). On the other hand, both marginal seas, ES and BS show stark different in air-sea flux; that in ES is even lower than in NP due to higher atmospheric CO concentration and weaker wind speed in ES. However, in BS dissolved [CO] was the highest among the three provinces and wind was strong. Even the air-sea fluxes observed near the Bering continental slope on July 25 were orders of magnitude higher than any other expedition period. Such a high outgassing rate has been reported in the productive regions, e.g. 22.8 μmol m^{-2} d^{-1} in central Pacific (Johnson and Bates, 1996), 4.6−9.6 μmol m^{-2} d^{-1} in Mauritanian upwelling (Kitidis et al., 2011), and 5 μmol m^{-2} d^{-1} in the northern California upwelling (Conte et al., 2019; Fichot and Benner, 2011; Armbrust, 2009; Bates et al., 2012).

Compared to the microbial oxidation (*M*), the outgassing by air-sea gas exchange plays a minor role as a sink; their fractions in the sink strength are merely from 0.9% in ES to 8% in NP (Table 2).

3.6.4 Vertical diffusion (*V*)

The vertical diffusion rate, *V*, relies on the eddy diffusivity and the gradient of dissolved CO concentration at the bottom of the mixed layer. Daily mean eddy diffusivities varied from 9.3×10^{-5} to 1.0×10^{-3} m^2 s^{-1}, increasing with latitude due to lesser stratification of the water column in the high latitudes. The vertical diffusion rate of dissolved CO at the bottom of the mixed layer was 0.62 μmol m^{-2} d^{-1} on average with the exception at Station 2 where *V* acted as a source of 0.5 μmol m^{-2} d^{-1} (Figure 5). The *V* term accounts for approximately 25% of the gas exchange rate and only 2% of the photochemical production of CO on average, demonstrating that the vertical diffusion is negligible for the marine CO cycle, as noted by Zafiriou et al. (2008).
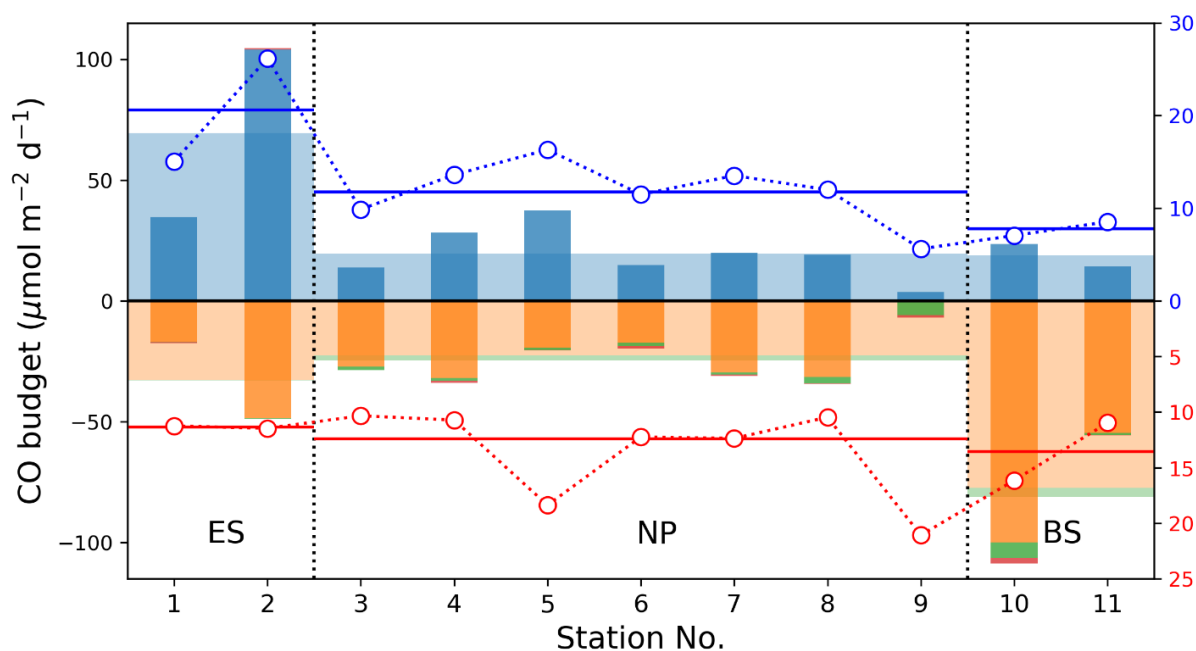
Figure 5: CO budget terms in the mixed layer at each station. Blue and red open circles indicate daily-integrated insolation and MLD, respectively, and their solid horizontal lines represent the mean values in the given provinces.

3.6.5 CO budget

According to a simple budget calculation by Eq (3), we estimated the CO budget in the surface mixed layer at each station (Figure 5). The CO budget was balanced in the open ocean, NP, but not in the marginal seas, ES and BS, although the large uncertainties in the budget terms leave room for potential balance. The CO cycle in ES was dominated by photochemical production, which was approximately twice as large as the entire sink strengths, while strong microbial oxidation in BS resulted in a net sink in the mixed layer of ~60 μmol m^{-2} day^{-1}, which is approximately three times larger than the photochemical production. Although the uncertainties in budget terms in ES and BS are fairly large, their mean values suggest that the CO cycles in ES and BS require external CO transport in the water column to stay in steady state during the observation period.

3.7 CO column burden

400   In general, [CO] exponentially decreases with depth in water column due to limited penetration of short-wavelength radiation that effectively stimulates the CO production (Conrad et al., 1982; Johnson and Bates, 1996; Kettle, 2005; Zafiriou et al., 2008). This typical depth-profile pattern was observed at the stations in NP, while the vertical [CO] profiles at stations in BS showed very low concentrations in MLD (~0.6 nM). In ES, [CO] remained around 1 nM even at the aphotic deep water without any vertical gradients (Figure 6a). Excluding Stations 1 and 2, the minimum and maximum CO concentrations in MLD were 0.80
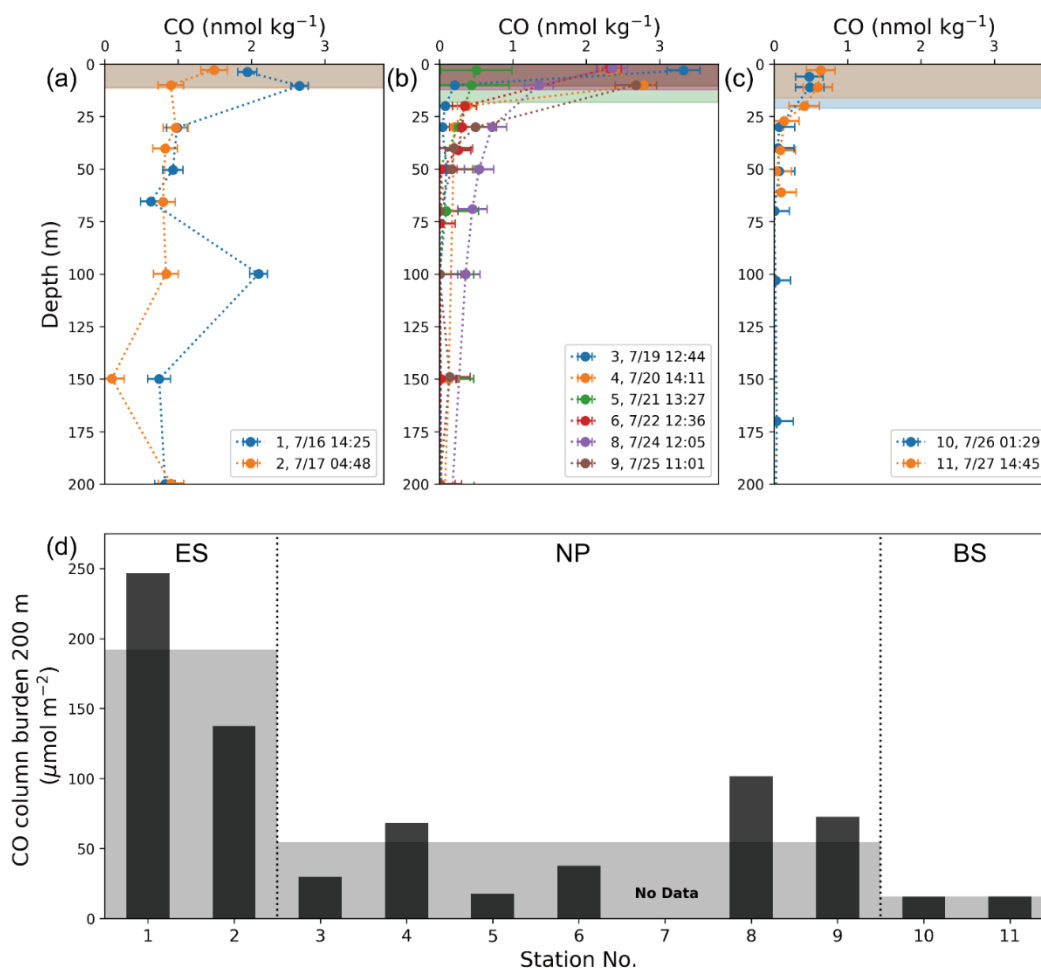
Figure 6: Vertical depth profiles of CO concentrations in (a) ES, (b) NP, and (c) BS provinces, and (d) their column burdens of CO down to 200 m deep (CB$_{200}$) at the stations. Shades in (a) to (c) indicate mixed layers at each station, and in (d) for the mean values of CB$_{200}$ in each province.

405    $\pm$ 0.19 nmol kg^{-1} (Station 10) and 3.32 $\pm$ 0.23 nmol kg^{-1} (Station 3), respectively, and the mean value was 1.83 nmol kg^{-1}. At depths deeper than 200 m, the CO concentrations converge toward the value less than detection limit (<0.2 nmol kg^{-1}).

The column burden of CO was calculated at each station by integrating the observed vertical profile of CO over 200 m depth (CB_{200}; Figure 6b). The mean CB_{200} values were 483.7 ($\pm$51.14) $\mu mol\ m^{-2}$ in ES, 66.0 ($\pm$27.1) $\mu mol\ m^{-2}$ in NP, and 13.2 ($\pm$1.2) $\mu mol\ m^{-2}$ in BS, drastically decreasing with latitude, contrary to the gradual increase of the surface CO concentration ($[CO]_{sea}$)

410 due likely to the decrease of insolation with the increasing latitutde. Our CB_{200} values in NP and BS are roughly similar to the values reported in oligotrophic areas. The CB_{200} from the Bermuda Atlantic Time-series Study (BATS) station was 95 $\mu mol\ m^{-2}$ in March and 39 $\mu mol\ m^{-2}$ in August (Zafiriou et al., 2008) and the CB_{200} within the Southern Pacific Gyre (SPG) was 51 $\mu mol\ m^{-2}$ in April (Johnson and Bates, 1996). In contrast, the large CB_{200} value in ES is of the same order of magnitude as the column burden of the productive Pacific Equatorial Upwelling (PEU) zone in December (283 $\mu mol\ m^{-2}$; Johnson and Bates

415 (1996)). In ES, the upper 30 m accounted for ~8% of CB_{200} on average, reflecting a relatively even distribution regardless of depth. In contrast, the upper 30 m in NP and BS accounted for ~47% and ~73% of the CB_{200}, respectively, indicating concentrated distributions within the upper layer.

The high CB_{200} in ES stations can be attributed to the active photochemical production driven by the high CDOM absorbance and insolation (Table 1). On the other hand, in NP, the production rate was approximately balanced with sink terms and the

420 CB_{200} showed intermediate values (Figures 5 and 6). Despite the extremely low J value, the CB_{200} at Station 9 was similar to that of the other stations in NP due to the low microbial oxidation rate (M). In BS where the removal rate was fairly high relative to the production rate, the CB_{200} was lowest, but did not reach to zero. We did not observe a significant correlation between the column burden integrated within the surface MLD (CB_{MLD}) and the CO budget based on Eq 2; however, we found the meaningful relationship between the CB_{200} and the CO budget as shown in Figure 7.

425
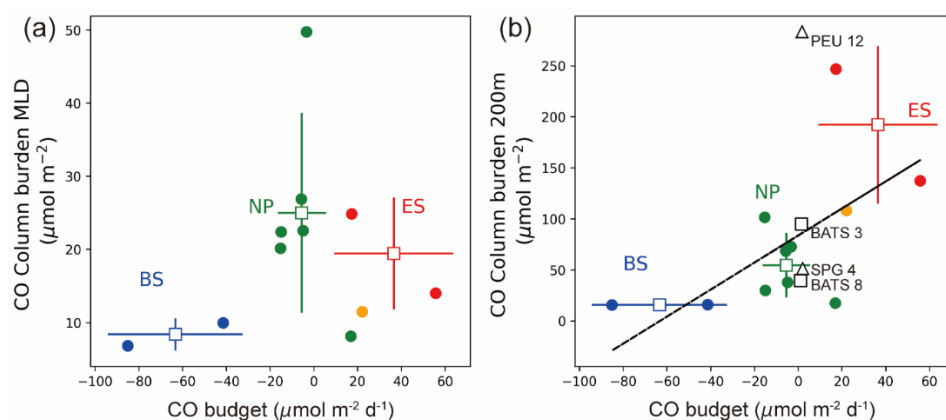
Figure 7: Comparison of CO column burdens (a) in the mixed layer (CB_{MLD}) and (b) from the surface down to 200 m deep (CB_{200}) against the CO budget in the mixed layer. In (b), black open squares and triangles are from Zafiriou et al. (2008) and Johnson and Bates (1996), respectively, where BATS 3 and 8 refer to Bermuda Atlantic Time-series Study in March and August, respectively,

430 **PEU 12 refers to Equatorial Pacific Upwelling region in December; and SPG 4 refers to South Pacific Gyre in April. Orange solid circle in (a) and (b) represents Station 12 off the coast of Nome, Alaska.**

4 Discussion

Although it is commonly assumed that the column burden is governed by biogeochemical budget, the CB_{MLD} values for the three provinces do not show any clear differences, and there is no relationship between CB_{MLD} and the CO budget in the mixed

435 layer (figure 7a). In contrast, CB_{200} is much higher than CB_{MLD} in ES, while CB_{200} is not much different from CB_{MLD} in BS. This results in a relatively clear relationship between the CO budget and CB_{200} (Figure 7b), which is counterintuitive since the relative magnitude of column burden should not change depending on the integration depth below MLD as the vertical turbulence diffusion is not a significant factor in the CO cycle (see Table 2).

Figure 7 provides insight into why high CB_{200} in ES may be due to the supply of CO from the sea surface by subduction, while

440 CO in BS could be supplied by surface lateral fluxes from hotspots of CO production. Given that 1) neither penetration of irradiance to depth deeper than 100 m nor vigorous vertical mixing overwhelming microbial oxidation are found in the province ES and 2) the fairly high ratio of source to sink strengths in the mixed layer (Figure 5) was not reflected in CB_{MLD}, but in CB_{200}, the vertically little varied distribution of high CO at the ES stations could be attributed to the subduction of high CO surface water. We hypothesize that the subduction of surface water is driven by warm core eddies, such as the Ulleung Warm Eddy

445 (UWE), which is derived from the warm core of its subsurface structure (Kim and Yoon, 1999) and originates from the East Korean Warm Current, a northward branch of the Tsushima Warm Current (Shin et al., 2005). Under the right convergent conditions that forms warm core eddies, warmer (and high CO) surface waters can converge and be down-welled to the depth deeper than 100 m depth. Given that several studies (Isoda and Saitoh, 1993; Capotondi et al., 2019; Ichiye and Takano, 1988) describe the eddies with the core temperature and salinity of 5−10°C and 34.1−34.3 near 200 m depth, Station 1 appears to be

450 located at the edge of a warm core eddy (Figure S3). This unique feature of a dynamic eddying flow field that subducts surface water with high concentrations of organic carbon and dissolved oxygen has also been observed in North Atlantic Ocean (Omand et al., 2015).

The behavior of CO in the province of BS appears to be influenced by lateral transports, as opposed to ES where subduction of high CO surface water might be responsible. In this area, [CO] remained above ~0.5 nM in the upper layers (Figure 6c)

455 although the total sink strengths were much higher than source strength. Moreover, a significant peak in surface [CO] was observed around Station 10 (Figure 2b) despite the small column burden of BS. These observations imply that the CO inventory in the water column cannot be fully explained only by the biogeochemical processes with Eulerian approach. Station 10 is located at the eastern boundary of the Aleutian Basin where the bottom depth is drastically altered (Figure 1). The Bering Slope Current (BSC; Kinder et al. (1975)) flows northwestwards along the slope passing through this station. At around 54°N,

460 167°W where the BSC starts, the Alaska Current (AC), which has high concentration of dissolved organic carbon (DOC) originated from Alaska coastal runoff, mixes with BSC (Chen et al., 2009). According to D'sa et al. (2014), the DOC concentrations is twice as high as the surrounding waters at this point. Given that the mean velocity of BSC is about 34 km d^{-1} (Ladd and Stabeno, 2009), this water of high photoproduction from replete organic carbon may potentially influence the area of Station 10. The sudden decrease of SSS right after passing through Station 10 also implies potential freshwater contribution.

465   Similarly, the column burden at Station 11 is comparable to other stations despite the higher sink strengths than the source strength, which can be explained by the lateral flux of high CO surface waters from the coastal region. Station 12, located near Station 11, is in the coastal area of Alaska (Figure 1) can be defined as an independent station not belonging to any provinces defined in this study. Aagaard et al. (2012) reported considerable horizontal shears and large lateral transports near Station 12 in the Bering Strait. The strong horizontal velocities and shallowness of the water columns can lead to interaction between

470   surface-forced and bottom-forced boundaries. We found that the water column of Station 12 is relatively well-mixed, as indicated by the CTD profiles of this station (Figure S3). While CB_{MLD} shows a low value (Figure 7a), the column burden over the total water column (~40 m) shows a high value comparable with the values of ES stations. Therefore, the high CO coastal water near Station 11 can be considered a source for high column burden relative to the low production rate of Station 11. The previous studies suggested that horizontal advection and lateral stirring across a front can drive much of the sub-mesoscale

475   heterogeneity in pCO$_2$ (Mahadevan et al., 2004). Other recent studies have also shown that lateral transport can explain the observed distribution of methane (CH$_4$) and dimethyl sulfide (DMS) in high latitude regions (Asher et al., 2011; Pohlman et al., 2017; Kim et al., 2017). Zafiriou et al. (2008) and Conte et al (2021) have also mentioned a potential influence of horizontal processes of different water masses on CO profiles in low latitude oligotrophic region. Given these studies, the horizontal transport could be one of explanations for the missing CO budget observed in this study.

480   In the province NP, the typical exponential features of vertical gradient in dissolved [CO] appeared well in all stations (Figure 6b). Strong decrease in [CO] occurred in the surface mixed layer indicating the photochemical degradation of CDOM following the penetration depth of short-wavelength radiation. Due to the broad spatial coverage of this province, however, there seems to be different physical influences at local scales. Particularly, the warm-core eddy signal was found at Station 8 like at Station 1 given that the CO concentrations at depth are also high at the station. The slight increase of SST and SSS when passing

485   through Station 8 (Figure 2f) imply the influence of warm-core eddy. Moreover, two large eddies formed at both sides of Station 8 in Figure 1 also suggests the strong potential of the influences of those eddies. This is evidenced by the largest value of CB_{200} at Station 8 among the stations in NP due to high dissolved [CO] in the water column, again pointing to the significant contribution of the lateral transport by subduction processes.

5 Summary and conclusions

490   Along the cruise track from the East Sea to the Bering Sea passing through the western limb of the North Pacific in summer 2012, we measured the concentration of CO and the relevant parameters in water columns for the first time. We divided the cruise track into three provinces, the East Sea (ES), the North Pacific (NP), and the Bering Sea (BS) and compared the CO cycles measured along the hydrographic stations. Photochemical production and microbial oxidation were the key drivers governing the CO budgets over the provinces while air-sea gas exchange and vertical transport play minor roles. The CO

495   budgets were not balanced in the marginal seas, ES and BS while that in the open ocean (NP) was in balance, elucidating the significant contribution of physical transport in the marginal seas and probably even in the open ocean in a local scale. The

imbalance of CO budget was further investigated by calculating the CO column burden. The CB_{200} was the highest in the East Sea due likely to subduction of high CO water into the intermediate depth as well as high production rate in the upper layers. The lowest CB_{200} in the Bering Sea stemmed from weak insolation and vigorous microbial oxidation. Despite greater removal than production, our observations suggests that lateral transports of high CO surface water supply CO in the surface layer in this area. The North Pacific, where production and oxidation rates were approximately in balance, showed the intermediate CB_{200} value. Depending on the geographical locations in NP, signatures of influences by the fluvial input or the strong vertical mixing were found. Our study suggests that the physical transport play a significant role in distributing CO in water columns, even in the open ocean, which should be considered in global ocean CO modelling.

Conflict of Interest

The authors declare that the research was conducted in the absence of any commercial or financial relationships that could be construed as a potential conflict of interest.

Author Contributions

YS conducted measurements of CO concentration and the oxidation rate constant during the research cruise and wrote the initial draft of the manuscript. TS developed the overall observational plan, designed the observation systems required for underway and discrete CO concentration measurements, and wrote the manuscript together with YS. HC provides CDOM data and HW helped interpret physical oceanography, provided crucial insights, and conducted physical modelling experiments to support our hypotheses. All authors participated in the manuscript's revision process and have approved the final submitted version.

Data availability

All the datasets used in this paper are available at kpdc.kopri.re.kr.

Acknowledgments

This study was supported by the research programs, Development of Marine Science Exploration Technology in Coastal Areas grant (PM63012) and Survey of Geology and Seabed Environmental Changes in the Arctic Ocean (KIMST 20210632) from the Ministry of Oceans and Fisheries in the Republic of Korea. All the datasets used in this paper are available at kpdc.kopri.re.kr.

References

Aagaard, K., Roach, A. T., and Schumacher, J. D.: On the wind-driven variability of the flow through Bering Strait, J. Geophys. Res. Oceans., 90, 7213-7221, 10.1029/JC090iC04p07213, 2012.

525 Armbrust, E. V.: The life of diatoms in the world's oceans, Nature, 459, 185-192, 10.1038/nature08057, 2009.

Asher, E. C., Merzouk, A., and Tortell, P. D.: Fine-scale spatial and temporal variability of surface water dimethylsufide (DMS) concentrations and sea–air fluxes in the NE Subarctic Pacific, Mar. Chem., 126, 63-75, 10.1016/j.marchem.2011.03.009, 2011.

Bates, T. S., Kelly, K. C., Johnson, J. E., and Gammon, R. H.: Regional and seasonal variations in the flux of oceanic carbon monoxide to the atmosphere, J Geophys Res-Atmos, 100, 23093-23101, 10.1029/95jd02737, 2012.

530 Bird, R. E. and Hulstrom, R. L.: Simplified clear sky model for direct and diffuse insolation on horizontal surfaces, Solar Energy Research Inst., Golden, CO (USA), 1981.

Bricaud, A., Morel, A., and Prieur, L.: Absorption by dissolved organic matter of the sea (yellow substance) in the UV and visible domains 1, Limnol. Oceanogr., 26, 43-53, 1981.

Brzezinski, M. A., Dickson, M.-L., Nelson, D. M., and Sambrotto, R.: Ratios of Si, C and N uptake by microplankton in the 535 Southern Ocean, Deep-Sea Res. II, 50, 619-633, 10.1016/s0967-0645(02)00587-8, 2003.

Capotondi, A., Jacox, M., Bowler, C., Kavanaugh, M., Lehodey, P., Barrie, D., Brodie, S., Chaffron, S., Cheng, W., Dias, D. F., Eveillard, D., Guidi, L., Iudicone, D., Lovenduski, N. S., Nye, J. A., Ortiz, I., Pirhalla, D., Pozo Buil, M., Saba, V., Sheridan, S., Siedlecki, S., Subramanian, A., de Vargas, C., Di Lorenzo, E., Doney, S. C., Hermann, A. J., Joyce, T., Merrifield, M., Miller, A. J., Not, F., and Pesant, S.: Observational Needs Supporting Marine Ecosystems Modeling and Forecasting: From 540 the Global Ocean to Regional and Coastal Systems, Front. Mar. Sci., 6, 10.3389/fmars.2019.00623, 2019.

Carder, K. L., Chen, F. R., Lee, Z. P., Hawes, S. K., and Kamykowski, D.: Semianalytic Moderate-Resolution Imaging Spectrometer algorithms for chlorophyll a and absorption with bio-optical domains based on nitrate-depletion temperatures, J. Geophys. Res. Oceans., 104, 5403-5421, 10.1029/1998jc900082, 1999.

Chen, J. L., Wilson, C. R., Blankenship, D., and Tapley, B. D.: Accelerated Antarctic ice loss from satellite gravity 545 measurements, Nat Geosci, 2, 859-862, 10.1038/ngeo694, 2009.

Conrad, R. and Seiler, W.: Photooxidative production and microbial consumption of carbon monoxide in seawater, FEMS Microbiol. Lett., 9, 61-64, 1980.

Conrad, R., Seiler, W., Bunse, G., and Giehl, H.: Carbon monoxide in seawater (Atlantic Ocean), J. Geophys. Res. Oceans., 87, 8839-8852, 1982.

550 Conte, L., Szopa, S., Séférian, R., and Bopp, L.: The oceanic cycle of carbon monoxide and its emissions to the atmosphere, Biogeosciences, 16, 881-902, 10.5194/bg-16-881-2019, 2019.

D'Sa, E. J., Goes, J. I., Gomes, H., and Mouw, C.: Absorption and fluorescence properties of chromophoric dissolved organic matter of the eastern Bering Sea in the summer with special reference to the influence of a cold pool, Biogeosciences, 11, 3225-3244, 10.5194/bg-11-3225-2014, 2014.

555 Daniel, J. S. and Solomon, S.: On the climate forcing of carbon monoxide, J. Geophys. Res., 103, 13249-13260, 1998.

de Boyer Montégut, C.: Mixed layer depth over the global ocean: An examination of profile data and a profile-based climatology, J. Geophys. Res., 109, 10.1029/2004jc002378, 2004.

Duarte, C. M. and Regaudie-de-Gioux, A.: Thresholds of gross primary production for the metabolic balance of marine planktonic communities, Limnol. Oceanogr., 54, 1015-1022, 10.4319/lo.2009.54.3.1015, 2009.

560 Edson, J. B., Jampana, V., Weller, R. A., Bigorre, S. P., Plueddemann, A. J., Fairall, C. W., Miller, S. D., Mahrt, L., Vickers, D., and Hersbach, H.: On the Exchange of Momentum over the Open Ocean, J. Phys. Oceanogr., 43, 1589-1610, 10.1175/jpo-d-12-0173.1, 2013.

Erickson III, D. J.: Ocean to atmosphere carbon monoxide flux: Global inventory and climate implications, Glob. Biogeochem. Cycles, 3, 305-314, 1989.

565 Fairall, C. W., Bradley, E. F., Hare, J. E., Grachev, A. A., and Edson, J. B.: Bulk Parameterization of Air–Sea Fluxes: Updates and Verification for the COARE Algorithm, J. Climate, 16, 571-591, 10.1175/1520-0442(2003)016<0571:Bpoasf>2.0.Co;2, 2003.

Fichot, C. G. and Benner, R.: A novel method to estimate DOC concentrations from CDOM absorption coefficients in coastal waters, Geophys Res Lett, 38, n/a-n/a, 10.1029/2010gl046152, 2011.

570 Fujiki, T., Matsumoto, K., Mino, Y., Sasaoka, K., Wakita, M., Kawakami, H., Honda, M. C., Watanabe, S., and Saino, T.: Seasonal cycle of phytoplankton community structure and photophysiological state in the western subarctic gyre of the North Pacific, Limnol. Oceanogr., 59, 887-900, 10.4319/lo.2014.59.3.0887, 2014.

Gnanadesikan, A.: Modeling the diurnal cycle of carbon monoxide: Sensitivity to physics, chemistry, biology, and optics, J Geophys Res-Oceans, 101, 12177-12191, 10.1029/96jc00463, 1996.

575 Green, S. A. and Blough, N. V.: Optical absorption and fluorescence properties of chromophoric dissolved organic matter in natural waters, Limnol Oceanogr, 39, 1903-1916, 10.4319/lo.1994.39.8.1903, 1994.

Ho, D. T., Wanninkhof, R., Schlosser, P., Ullman, D. S., Hebert, D., and Sullivan, K. F.: Toward a universal relationship between wind speed and gas exchange: Gas transfer velocities measured with3He/SF6during the Southern Ocean Gas Exchange Experiment, J. Geophys. Res., 116, 10.1029/2010jc006854, 2011.

580 Ichiye, T. and Takano, K.: Mesoscale eddies in the Japan Sea, La mer, 26, 69-75, 1988.

Isobe, A.: Freshwater and temperature transports through the Tsushima-Korea Straits, J Geophys Res-Oceans, 107, 2-1-2-20, 10.1029/2000jc000702, 2002.

Isoda, Y. and Saitoh, S.-i.: The northward intruding eddy along the East coast of Korea, J. Oceanogr., 49, 443-458, 10.1007/bf02234959, 1993.

585 Johnson, J. E. and Bates, T. S.: Sources and sinks of carbon monoxide in the mixed layer of the tropical South Pacific Ocean, Glob. Biogeochem. Cycles, 10, 347-359, 10.1029/96gb00366, 1996.

Jones, R. D.: Carbon monoxide and methane distribution and consumption in the photic zone of the Sargasso Sea, Deep-Sea Res, 38, 625-635, 10.1016/0198-0149(91)90002-w, 1991.

Jones, R. D. and Amador, J. A.: Methane and carbon monoxide production, oxidation, and turnover times in the Caribbean
590 Sea as influenced by the Orinoco River, J Geophys Res-Oceans, 98, 2353-2359, 10.1029/92jc02769, 2012.

Kawai, H.: Hydrography of the Kuroshio extension, Kuroshio-Its Physical Aspects, 1972.

Kettle, A. J.: Comparison of the nonlocal transport characteristics of a series of one-dimensional oceanic boundary layer models, Ocean Model, 8, 301-336, 10.1016/j.ocemod.2004.01.002, 2005.

Kim, C.-H. and Yoon, J.-H.: Modeling of the wind-driven circulation in the Japan Sea using a reduced gravity model, J.
595 Oceanogr., 52, 359-373, 10.1007/bf02235930, 1996.

Kim, C.-H. and Yoon, J.-H.: A Numerical Modeling of the Upper and the Intermediate Layer Circulation in the East Sea, J. Oceanogr., 55, 327-345, 10.1023/a:1007837212219, 1999.

Kim, I., Hahm, D., Park, K., Lee, Y., Choi, J. O., Zhang, M., Chen, L., Kim, H. C., and Lee, S.: Characteristics of the horizontal and vertical distributions of dimethyl sulfide throughout the Amundsen Sea Polynya, 584-585, 154-163,
600 10.1016/j.scitotenv.2017.01.165, 2017.

Kinder, T. H., Coachman, L. K., and Galt, J. A.: The Bering Slope Current System, J. Phys. Oceanogr., 5, 231-244, 10.1175/1520-0485(1975)005<0231:Tbscs>2.0.Co;2, 1975.

Kitidis, V., Tilstone, G. H., Smyth, T. J., Torres, R., and Law, C. S.: Carbon monoxide emission from a Mauritanian upwelling filament, Mar Chem, 127, 123-133, 10.1016/j.marchem.2011.08.004, 2011.

605 Kitidis, V., Stubbins, A. P., Uher, G., Upstill Goddard, R. C., Law, C. S., and Woodward, E. M. S.: Variability of chromophoric organic matter in surface waters of the Atlantic Ocean, Deep-Sea Res. II, 53, 1666-1684, 10.1016/j.dsr2.2006.05.009, 2006.

Kowalczuk, P., Zabłocka, M., Sagan, S., and Kuliński, K.: Fluorescence measured in situ as a proxy of CDOM absorption and DOC concentration in the Baltic Sea, Oceanologia, 52, 431-471, 10.5697/oc.52-3.431, 2010.

Kuroda, H., Suyama, S., Miyamoto, H., Setou, T., and Nakanowatari, T.: Interdecadal variability of the Western Subarctic
610 Gyre in the North Pacific Ocean, Deep-Sea Res. I, 169, 103461, 10.1016/j.dsr.2020.103461, 2021.

Kwak, J. H., Hwang, J., Choy, E. J., Park, H. J., Kang, D.-J., Lee, T., Chang, K.-I., Kim, K.-R., and Kang, C.-K.: High primary productivity and f-ratio in summer in the Ulleung basin of the East/Japan Sea, Deep-Sea Res. I, 79, 74-85, 10.1016/j.dsr.2013.05.011, 2013.

Kwon, E. Y., DeVries, T., Galbraith, E. D., Hwang, J., Kim, G., and Timmermann, A.: Stable Carbon Isotopes Suggest Large
615 Terrestrial Carbon Inputs to the Global Ocean, Glob. Biogeochem. Cycles, 35, e2020GB006684, 10.1029/2020gb006684, 2021.

Ladd, C. and Stabeno, P. J.: Freshwater transport from the Pacific to the Bering Sea through Amukta Pass, Geophys. Res. Lett., 36, 10.1029/2009gl039095, 2009.

Levy, H., 2nd: Normal atmosphere: large radical and formaldehyde concentrations predicted, Science, 173, 141-143,
10.1126/science.173.3992.141, 1971.

Li, H.-M., Zhang, C.-S., Han, X.-R., and Shi, X.-Y.: Changes in concentrations of oxygen, dissolved nitrogen, phosphate, and silicate in the southern Yellow Sea, 1980–2012: Sources and seaward gradients, Estuar. Coast. Shelf Sci., 163, 44-55, 10.1016/j.ecss.2014.12.013, 2015.

Mahadevan, A., Lévy, M., and Mémery, L.: Mesoscale variability of sea surface pCO2: What does it respond to?, Glob. Biogeochem. Cycles, 18, 2004.

Mannino, A., Novak, M. G., Hooker, S. B., Hyde, K., and Aurin, D.: Algorithm development and validation of CDOM properties for estuarine and continental shelf waters along the northeastern U.S. coast, Remote Sens. Environ., 152, 576-602, 10.1016/j.rse.2014.06.027, 2014.

Mathis, J. T., Hansell, D. A., and Bates, N. R.: Strong hydrographic controls on spatial and seasonal variability of dissolved organic carbon in the Chukchi Sea, Deep-Sea Res. II, 52, 3245-3258, 10.1016/j.dsr2.2005.10.002, 2005.

Miller, W. L., Moran, M., Sheldon, W. M., Zepp, R. G., and Opsahl, S.: Determination of apparent quantum yield spectra for the formation of biologically labile photoproducts, Limnol Oceanogr, 47, 343-352, 10.4319/lo.2002.47.2.0343, 2002.

Mopper, K. and Kieber, D.: Marine photochemistry and its impact on carbon cycling, in: The effects of UV radiation in the marine environment, 101-129, 2000.

Morimoto, A., Takikawa, T., Onitsuka, G., Watanabe, A., Moku, M., and Yanagi, T.: Seasonal variation of horizontal material transport through the eastern channel of the Tsushima Straits, J Oceanogr, 65, 61-71, 10.1007/s10872-009-0006-z, 2009.

Nightingale, P. D., Malin, G., Law, C. S., Watson, A. J., Liss, P. S., Liddicoat, M. I., Boutin, J., and Upstill-Goddard, R. C.: In situ evaluation of air-sea gas exchange parameterizations using novel conservative and volatile tracers, Glob. Biogeochem. Cycles, 14, 373-387, 10.1029/1999gb900091, 2000.

Ohta, K.: Diurnal Variations of Carbon Monoxide Concentration in the Equatorial Pacific Upwelling Region, J. Oceanogr., 53, 173-178, 1997.

Omand, M. M., D'Asaro, E. A., Lee, C. M., Perry, M. J., Briggs, N., Cetinic, I., and Mahadevan, A.: Eddy-driven subduction exports particulate organic carbon from the spring bloom, Science, 348, 222-225, 10.1126/science.1260062, 2015.

Park, K. and Rhee, T. S.: Source characterization of carbon monoxide and ozone over the Northwestern Pacific in summer 2012, Atmos. Environ., 111, 151-160, 2015.

Park, K. and Rhee, T. S.: Oceanic source strength of carbon monoxide on the basis of basin-wide observations in the Atlantic, Environ. Sci. Process. Impacts, 18, 104-114, 10.1039/c5em00546a, 2016.

Parsons, T., Maita, Y., and Lalli, C.: A manual of chemical and biological methods for seawater analysis.–Pergamon Press, Oxford, 173 pp, 1984.

Pohlman, J. W., Greinert, J., Ruppel, C., Silyakova, A., Vielstadte, L., Casso, M., Mienert, J., and Bunz, S.: Enhanced CO(2) uptake at a shallow Arctic Ocean seep field overwhelms the positive warming potential of emitted methane, PNAS, 114, 5355-5360, 10.1073/pnas.1618926114, 2017.

Rhee, T. S.: The process of air-water gas exchange and its application, Texas A&M University College Station, Texas, USA, 2000.

Rhee, T. S., Nightingale, P. D., Woolf, D. K., Caulliez, G., Bowyer, P., and Andreae, M. O.: Influence of energetic wind and waves on gas transfer in a large wind–wave tunnel facility, J. Geophys. Res., 112, 10.1029/2005jc003358, 2007.

Seiler, W.: The cycle of atmospheric CO, 26, 116-135, 1974.

Shin, H.-R., Shin, C.-W., Kim, C., Byun, S.-K., and Hwang, S.-C.: Movement and structural variation of warm eddy WE92 for three years in the Western East/Japan Sea, Deep-Sea Res. II, 52, 1742-1762, 10.1016/j.dsr2.2004.10.004, 2005.

Sikorski, R. J. and Zika, R. G.: Modeling mixed-layer photochemistry of H2O2: Optical and chemical modeling of production, J Geophys Res-Oceans, 98, 2315-2328, 10.1029/92jc02933, 2012.

Smith, S. R., Bourassa, M. A., and Sharp, R. J.: Establishing More Truth in True Winds, J. Atmos. Oceanic Technol., 16, 939-952, 10.1175/1520-0426(1999)016<0939:Emtitw>2.0.Co;2, 1999.

Stabeno, P. J. and Reed, R.: Circulation in the Bering Sea basin observed by satellite-tracked drifters: 1986–1993, J. Phys. Oceanogr., 24, 848-854, 1994.

Stabeno, P. J., Schumacher, J. D., and Ohtani, K.: The physical oceanography of the Bering Sea, in: Dynamics of the Bering Sea, 1-28, 1999.

Stubbins, A., Law, C. S., Uher, G., and Upstill-Goddard, R. C.: Carbon monoxide apparent quantum yields and photoproduction in the Tyne estuary, Biogeosciences, 8, 703-713, 10.5194/bg-8-703-2011, 2011.

670 Stubbins, A., Uher, G., Kitidis, V., Law, C. S., Upstill-Goddard, R. C., and Woodward, E. M. S.: The open-ocean source of atmospheric carbon monoxide, Deep-Sea Res. II, 53, 1685-1694, 10.1016/j.dsr2.2006.05.010, 2006.

Takao, S., Iida, T., Isada, T., Saitoh, S.-I., Hirata, T., and Suzuki, K.: Bio-optical properties during the summer season in the Sea of Okhotsk, Prog. Oceanogr., 126, 233-241, 10.1016/j.pocean.2014.04.010, 2014.

Twardowski, M. S., Boss, E., Sullivan, J. M., and Donaghay, P. L.: Modeling the spectral shape of absorption by chromophoric

675 dissolved organic matter, Mar Chem, 89, 69-88, 10.1016/j.marchem.2004.02.008, 2004.

Vodacek, A., Blough, N. V., DeGrandpre, M. D., DeGrandpre, M. D., and Nelson, R. K.: Seasonal variation of CDOM and DOC in the Middle Atlantic Bight: Terrestrial inputs and photooxidation, Limnol Oceanogr, 42, 674-686, 10.4319/lo.1997.42.4.0674, 1997.

Walvoord, M. A. and Striegl, R. G.: Increased groundwater to stream discharge from permafrost thawing in the Yukon River

680 basin: Potential impacts on lateral export of carbon and nitrogen, Geophys Res Lett, 34, 10.1029/2007gl030216, 2007.

Wanninkhof, R.: Relationship between wind speed and gas exchange over the ocean, J Geophys Res-Oceans, 97, 7373-7382, 10.1029/92jc00188, 2012.

Wanninkhof, R.: Relationship between wind speed and gas exchange over the ocean revisited, Limnol. Oceanogr. Methods, 12, 351-362, 10.4319/lom.2014.12.351, 2014.

685 Weinstock, B. and Niki, H.: Carbon monoxide balance in nature, Science, 176, 290-292, 10.1126/science.176.4032.290, 1972.

Wiesenburg, D. A. and Guinasso, N. L.: Equilibrium solubilities of methane, carbon monoxide, and hydrogen in water and sea water, J. Chem. Eng. Data, 24, 356-360, 10.1021/je60083a006, 2002.

Xie, H., Zafiriou, O. C., Umile, T. P., and Kieber, D. J.: Biological consumption of carbon monoxide in Delaware Bay, NW Atlantic and Beaufort Sea, Mar Ecol Prog Ser, 290, 1-14, 10.3354/meps290001, 2005.

690 Yamamoto-Kawai, M., Carmack, E., and McLaughlin, F.: Nitrogen balance and Arctic throughflow, Nature, 443, 43, 10.1038/443043a, 2006.

Yamashita, Y., Cory, R. M., Nishioka, J., Kuma, K., Tanoue, E., and Jaffé, R.: Fluorescence characteristics of dissolved organic matter in the deep waters of the Okhotsk Sea and the northwestern North Pacific Ocean, Deep-Sea Res. II, 57, 1478-1485, 10.1016/j.dsr2.2010.02.016, 2010.

695 Yasuda, I.: The origin of the North Pacific Intermediate Water, J. Geophys. Res. Oceans., 102, 893-909, 10.1029/96jc02938, 1997.

Yasuda, I.: Hydrographic Structure and Variability in the KuroshioOyashio Transition Area, J. Oceanogr., 389-402, 2003.

Zafiriou, O. C., Andrews, S. S., and Wang, W.: Concordant estimates of oceanic carbon monoxide source and sink processes in the Pacific yield a balanced global "blue-water" CO budget, Glob. Biogeochem. Cycles, 17, 10.1029/2001gb001638, 2003.

700 Zafiriou, O. C., Xie, H., Nelson, N. B., Najjar, R. G., and Wang, W.: Diel carbon monoxide cycling in the upper Sargasso Sea near Bermuda at the onset of spring and in midsummer, Limnol Oceanogr, 53, 835-850, 10.4319/lo.2008.53.2.0835, 2008.